**PAPER**

Check for updates

# UV-spectrum and photodecomposition of peroxynitrous acid in the troposphere†

Wiem Chebbi, [ID] *[ab] Najoua Derbel, [ID] [a] Alexander Alijah [ID] [b] and Thibaud Cours [ID] [b]

The UV spectrum of peroxynitrous acid, HOONO, was computed at the B3LYP/AVTZ and MCSCF/AVTZ levels using the fewest switches surface hopping algorithm. Due to large-amplitude vibrational motions of this molecule, the maxima in the simulated spectra are displaced from the positions of vertical excitations. The three lowest excited electronic singlet states, which are all repulsive, can be reached by UV absorption. The photolysis products are determined, and the photolysis rate constant is provided for the first time. We found that near the tropopause the photolysis rate constant $J \approx 6 \times 10^{-4} \text{ s}^{-1}$, exceeds that for thermal decomposition by two orders of magnitude. The photolysis lifetime is about 30 minutes. Thus, photolysis is an important process and should be included in atmospheric models.

## 1 Introduction

Radicals containing hydrogen, OH and OOH, and nitrogen, NO and $NO_2$, are present in the earth's atmosphere where they participate in a large number of radical chain reactions.[1] More than fifty years ago, Crutzen[2] suggested that nitrogen oxides arriving in the stratosphere due to anthropogenic activities contribute to the catalytic conversion of ozone into dioxygen, thus damaging the stratospheric ozone layer. The nitrogen oxides can be removed partially from this cycle by recombination with the hydroxyl radical in the presence of a third body, such as $N_2$, $O_2$[3,4] or water.[5]

$$HO + NO_2 + M \rightarrow HONO_2 + M \qquad (1)$$

$$\rightleftharpoons HOONO + M \qquad (2)$$

Whereas the formation of nitric acid neutralises $NO_2$ and is indeed its predominant sink pathway in the troposphere; the alternative reaction leading to peroxynitrous acid is reversible, and peroxynitrous acid formed at low temperatures at night may decompose during daytime. The formation of peroxynitrous acid constitutes a minor channel at low pressures, for which Bean *et al.*[6] reported a yield of 7.5 ± 2% at $p = 20$ torr. This increases to about 20% under standard conditions, as estimated by Golden *et al.*[7] through Master equation modelling

of experimental data, in particular those from Hippler's group.[8] Accurate determination of the overall rate constant and branching ratio of the above reaction is a hot topic of research, see for example Mollner, Amedro, Winiberg and coworkers[5,9,10] and references therein. Peroxynitrous acid can be converted to some extent into nitric acid. The mechanism was reported in ref. 11 and 12.

Peroxynitrous acid, known for a long time to exist in aqueous solution,[13] was first isolated in an argon matrix by Y. P. Lee's group[14,15] and identified by IR spectroscopy. In their experiment, the acid was formed by recombination of the photolysis products of nitric acid. They also recorded the UV spectrum[16] of peroxynitrous acid. Identification of this molecule was guided by theoretical predictions provided by McGrath *et al.*[17] More recently, Zhang and coworkers[18,19] reported the experimental vibrational overtone spectrum of the matrix-isolated *cis–cis* conformer, supported by *ab initio* computations. First experimental evidence for the existence of peroxynitrous acid in the gas phase was provided by Donahue *et al.*[20] and by Hippler *et al.*,[8] when they studied the kinetics of the OH + $NO_2$ reaction. The molecule was then observed directly in the gas phase by Nizkorodov and Wennberg[21] by vibrational photodissociation spectroscopy, following excitation of the OH stretching mode. In another overtone action-spectroscopic experiment, Pollack *et al.*[22] identified the less stable *trans*-perp conformer. Fry *et al.*[23] also detected the *trans*-perp conformer and noticed rapid isomerization to the more stable *cis–cis* conformer. Bean and coworkers,[6] in a kinetics study carried out in a low-pressure discharge flow reactor, observed both peroxynitrous acid in the *cis–cis* conformation and nitric acid by infrared cavity ringdown spectroscopy. Experimental and computational evidence for the existence of a third conformer, called *cis*-perp, was presented by Li *et al.*[24] Drouin, Fry and Miller[25,26] investigated the *cis–cis*

*a LSAMA, Laboratoire de Spectroscopie Atomique, Moléculaire et Applications, Department of Physics, University Tunis - El Manar, 1060 Tunis, Tunisia*

*b GSMA, Groupe de Spectrométrie Moléculaire et Atmosphérique, UMR CNRS 7331, University of Reims Champagne-Ardenne, 51100 Reims, France. E-mail: wiem.chebbi@univ-reims.fr*

† Electronic supplementary information (ESI) available: Figure of the *trans*-perp enantiomers, plot of orbitals, and parameters of Newton-X calculations. See DOI: https://doi.org/10.1039/d3cp04580c
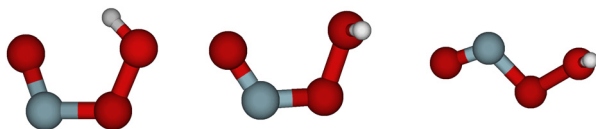
This journal is © the Owner Societies 2024

*Phys. Chem. Chem. Phys.*, 2024, **26**, 123–129 | **123**

**Fig. 1** Structures of the *cis–cis*, *cis*-perp and *trans*-perp configurations, from left to right.

conformer by submillimeter spectroscopy and derived rotational constants.

Substantial theoretical work was also published. The first thorough investigation of the potential energy surface was reported by McGrath and coworkers,[17,27] who also proposed a nomenclature for the structures of the stationary points on the potential energy surface. The most stable geometrical configuration of HOONO is the one classified as *cis–cis*, where both the OONO and the HOON entities are in *cis*-positions, see Fig. 1. This structure is stabilized by a hydrogen bond. There are two other local minima on the potential energy surface, denoted as *trans*-perp and *cis*-perp, as shown in Fig. 1. The *cis*-perp conformer is separated from the *cis–cis* conformer by a very weak rotational barrier.[28] The potential energy surface and geometrical structures of these conformers and transition states were studied by a number of authors, see for example., ref. 23, and 28–33 Accurate thermochemical data were reported by Szakács and coworkers.[34] In thermal equilibrium at room temperature, only the *cis–cis* conformer is populated. A global potential energy surface in full dimensionality was constructed by Chen *et al.*[33] and used for trajectory calculations.

The success of overtone action spectroscopy has stimulated theoretical investigations of excited rovibrational states and vibrational transition dipole moments.[24,35–38] Such calculations are non-trivial due to the presence of three low-frequency vibrational modes, the HO–ONO and HOO–NO torsional modes and the ONO bending vibration, and multidimensional models were devised for their description.[24,37,39]

In contrast to the impressive work on the characterisation of the ground state potential energy surface, vibrational spectroscopy and kinetic modelling, the electronic spectroscopy of peroxynitrous acid has received very little attention. The UV spectrum of peroxynitrous acid in an argon matrix was recorded almost forty years ago by W.-J. Lo and Y. P. Lee.[16] We are aware of a single theoretical publication, by Li and Francisco,[40] who investigated the *cis–cis* conformer and computed the vertical transition energies to the three lowest excited singlet states and two triplet states. Tentative assignment of the experimental bands was made on the basis of these transition energies. An important conclusion was that peroxynitrous acid, once formed in the atmosphere, will likely be photolysed. The aim of the present work is to re-analyse the experimental UV spectrum and to compute the photolysis rate constant under conditions found in the atmosphere near and above the tropopause. Such data are required for atmospheric modelling.[7,10,41]

## 2 UV spectrum

W.-J. Lo and Y. P. Lee,[15] studying the photolysis of nitric acid, $HONO_2$, in a solid argon matrix, observed the subsequent formation of peroxynitrous acid in the *cis–cis* and *trans*-perp configurations by recombination of the fragments according to reaction (2). They also recorded the IR[15] and UV spectra[16] of peroxynitrous acid. The latter spectra were reported in the range of 200 nm $< \lambda <$ 450 nm and show broad absorption signals that were attributed to the *cis–cis* and the *trans*-perp conformers. No further experiments have been conducted to the best of our knowledge.

To gain insight into the observed spectra, we have computed the oscillator strengths for electronic transitions from the ground state to the lowest three excited singlet state at the MCSCF/AVTZ level using the Molpro package.[42] Two active spaces were tested: a large active space CAS(24e,17o), *i.e.* 24 electrons of the valence shell in 17 active orbitals. Only the 1s orbitals of the heavy atoms were kept inactive. The other active space was CAS(16e,13o), in which also the 2s orbitals were kept inactive‡. A second set of computations were performed with Gaussian G16[43] at the density functional level with the same AVTZ basis set for comparison. The B3LYP functional was chosen after a systematic test with a number of alternative density functionals, M05-2X and M06-2X, as it produces reasonably well the relative intensities found in the experiment for the two isomers. The B3LYP functional has been widely used by previous workers. We note here that Berski and coworkers,[44] examining the electronic structure and bonding properties of this molecule with the same functionals, found that only B3LYP produces the geometrical structures correctly. The global potential energy surface presented by Chen *et al.*[33] is also based on the B3LYP functional.

The results of the two sets of computations are compared in Table 1. They are quite close, except for the transition to the third electronic state in the case of the *trans*-perp conformer. The reason is that the excitation energies of the *trans*-perp conformer are very sensible to the position of the hydrogen atom. The transitions are analysed in detail in Table 2. The most intense transition is towards the second excited electronic state, where the principal electronic excitation is between two $\pi$ orbitals and parallel to the molecular plane. Transitions to the first and third electronic states are $\sigma \rightarrow \pi$ and $\pi \rightarrow \sigma$ excitations, respectively, perpendicular to the molecular plane and thus less intense. As can be inferred from Table 2, the $\sigma$ or $\pi$ character of the HOMO, orbital 16, is changed when passing from the *cis–cis* configuration to the *trans*-perp configuration. This can be rationalised in the following way: in the planar *cis–cis* configuration, the hydrogen 1s-orbital cannot participate at the molecular $3\pi$ orbital by symmetry. As the hydrogen atom is rotated out of plane, its 1s orbital interacts strongly with the $\pi$ orbital at the oxygen atom so that the molecular $3\pi$ orbital becomes stabilized and passes below the $13\sigma$ orbital.

However, the vertical transition energies and oscillator strengths can only give a crude approximation to the UV spectrum of the title molecule, because the molecule is not static but performs large-amplitude torsional motions. For a more realistic simulation of the UV spectrum, displacement of

---

‡ Figures of the orbitals are provided as supplementary information.

**124** | *Phys. Chem. Chem. Phys.*, 2024, **26**, 123–129

This journal is © the Owner Societies 2024

**Table 1** Energies and oscillator strengths for excitations from the electronic ground state. The AVTZ basis set was used in all calculations

| Transition | B3LYP | | | MCSCF, CAS(16e,13o) | | | MCSCF, CAS(24e,17o) | | |
|---|---|---|---|---|---|---|---|---|---|
| | $E$ (eV) | $\lambda$ (nm) | $f$ | $E$ (eV) | $\lambda$ (nm) | $f$ | $E$ (eV) | $\lambda$ (nm) | $f$ |
| *cis–cis* | | | | | | | | | |
| $1 \rightarrow 2$ | 4.097 | 302.6 | 0.0020 | 4.181 | 296.5 | 0.0035 | 4.142 | 299.3 | 0.0027 |
| $1 \rightarrow 3$ | 5.114 | 242.5 | 0.0393 | 5.577 | 222.3 | 0.0292 | 5.505 | 225.2 | 0.0265 |
| $1 \rightarrow 4$ | 5.932 | 209.0 | 0.0004 | 5.896 | 210.3 | 0.0013 | 5.958 | 208.1 | 0.0010 |
| *trans*-perp | | | | | | | | | |
| $1 \rightarrow 2$ | 3.215 | 385.6 | 0.0010 | 3.478 | 356.4 | 0.0022 | 3.351 | 370.0 | 0.0016 |
| $1 \rightarrow 3$ | 5.212 | 237.9 | 0.0252 | 6.066 | 206.4 | 0.0340 | 5.637 | 219.9 | 0.0349 |
| $1 \rightarrow 4$ | 5.623 | 220.5 | 0.0017 | 7.381 | 156.5 | 0.0016 | 7.116 | 174.2 | 0.0010 |

the nuclei from their equilibrium positions needs to be taken into account. Such a simulation was performed using the Newton-X package[45] coupled to Gaussian G16.[43] Within Newton-X, the photoabsorption cross-section is computed as

$$\sigma(\lambda) = \frac{\pi e^2}{2 m_e c \varepsilon_0} \sum_{l \neq i}^{N_{fs}} \left[ \frac{1}{N_p^l} \sum_k^{N_p^l} f_{il}(\mathbf{x}_k) g(E - \Delta E_{il}(\mathbf{x}_k), \delta) \right] \quad (3)$$

In the above equation, $e$ denotes the elementary charge, $m_e$ is the electron mass, $c$ is the speed of light and $\varepsilon_0$ is the vacuum permittivity. $E = hc/\lambda$ is the radiation energy. $f_{il}$ is the oscillator strength for transitions between the initial electronic state i and the final state l, and $\Delta E_{il}$ is the corresponding transition energy. The outer summation is over final excited states. The inner sum samples the nuclear configurations, $\mathbf{x}_k$, obtained as deviations from a reference configuration along the normal modes and weighted by a Wigner distribution. Finally, $g$ is a Gaussian line shape function with a broadening of $\delta = 0.06$ eV, which is large enough to remove statistical noise, as described in detail by Barbatti *et al.*[46]

The computed UV spectra of the two isomers are presented in Fig. 2. Though the maxima of the signals are displaced from the experimental positions, which are $275 \pm 35$ nm for the *cis–cis* conformer and 220 nm for the *trans*-perp conformer, the spectra allow a useful analysis of the experimental results.

After irradiation of the argon matrix with a 308 nm source during one hour, while observing the IR spectrum, the signals of the *cis–cis* conformer became nearly unobservable, whereas those of the *trans*-perp conformer were still present. Our computed UV spectrum shows that radiation with a 308 nm laser reaches the first excited electronic state. This wavelength is close to the maximum of the signal for the *cis–cis* conformer, but is in the tail region of the signal for the *trans*-perp

conformer, which therefore decomposes slower than the *cis–cis* conformer.

Looking now at the intense signals, we note that they are very broad, which is likely caused by torsional motion. To analyse this finding, we have computed, at the MCSCF/AVTZ level, the vertical excitation energies as a function of the two torsional angles, and they are shown in Fig. 3. The *cis–cis* conformer is located at the centre of the figure. When either of the two torsional modes, NOOH or ONOO, is excited, the molecule samples nuclear configurations at which the vertical transition energies towards the first excited state are red-shifted. In contrast, excitation energies towards the second and third electronic states appear blue-shifted by the NOOH mode and red-shifted by the ONOO mode. As a consequence, the maximum for excitation to the first excited state is found around 330 nm, whereas the vertical excitation value is 300 nm. The signals for excitations to the second and third excited states, are broadened, but not displaced strongly from the vertical excitation value due to the counteracting effects of the two torsional motions. In the case of the *trans*-perp conformer, located at $\tau_{ONOO} \approx \pm 180°$ and $\tau_{NOOH} \approx \pm 90°$, excitation to the first excited state is close to the vertical excitation energy, as the two torsional motions counteract each other. However, these motions largely broaden the signal. Concerning excitation to the second or third excited states, both torsional motions shift the maximum of the signals towards larger wavelengths.

# 3 Photodecomposition

The thermal decomposition of HOONO on the electronic ground state surface was investigated by Dixon *et al.*[11] HOONO can break up mainly in two ways, HOONO $\rightarrow$ HO + NO$_2$ and HOONO $\rightarrow$ HO$_2$ + NO with energies of $\Delta E = 6925$ cm$^{-1}$ and 9548 cm$^{-1}$ with respect to the *cis–cis* conformer, though a third

**Table 2** Analysis of the UV spectrum for transitions from the electronic ground state of the *cis–cis* and *trans*-perp isomers to the lowest three excited singlet states computed at the B3LYP/AVTZ level

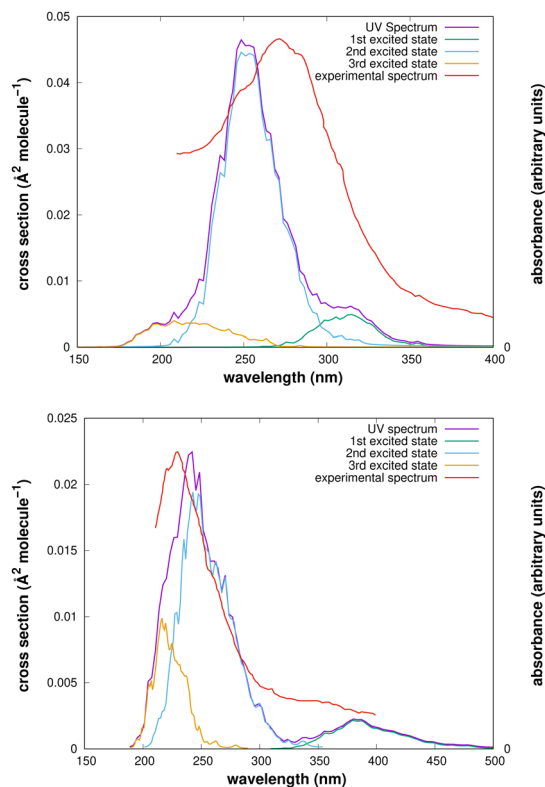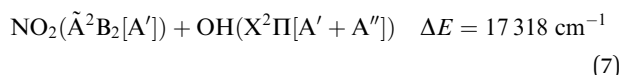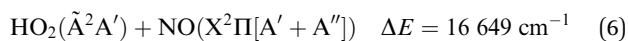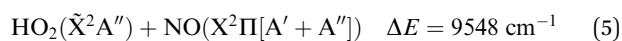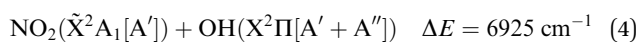| Transition | Cis–cis | | Trans-perp | |
|---|---|---|---|---|
| | Orbitals | Contribution [%] | Orbitals | Contribution [%] |
| $1 \rightarrow 2$ | 15 (13$\sigma$) $\rightarrow$ 17 (4$\pi$) | 71 | 16 (13 $\sigma$) $\rightarrow$ 17 (4$\pi$) | 71 |
| $1 \rightarrow 3$ | 16 (3$\pi$) $\rightarrow$ 17 (4$\pi$) | 68 | 15 (3$\pi$) $\rightarrow$ 17 (4$\pi$) | 66 |
| | 15 (13 $\sigma$) $\rightarrow$ 18 (14$\sigma$) | 15 | 16 (13 $\sigma$) $\rightarrow$ 20 (16$\sigma$) | 15 |
| $1 \rightarrow 4$ | 16 (3$\pi$) $\rightarrow$ 18 (14$\sigma$) | 70 | 14 (12 $\sigma$) $\rightarrow$ 17 (4$\pi$) | 66 |

**Fig. 2** UV spectrum and its decomposition in terms of electric states, computed at the B3LYP/AVTZ level. Upper: *cis–cis* and lower: *trans*-perp. Different axis scales were noted. As the experimental data were given in arbitrary units, they were scaled to match the maximum heights for each conformer, with scaling factors of 0.042 and 0.022 respectively.
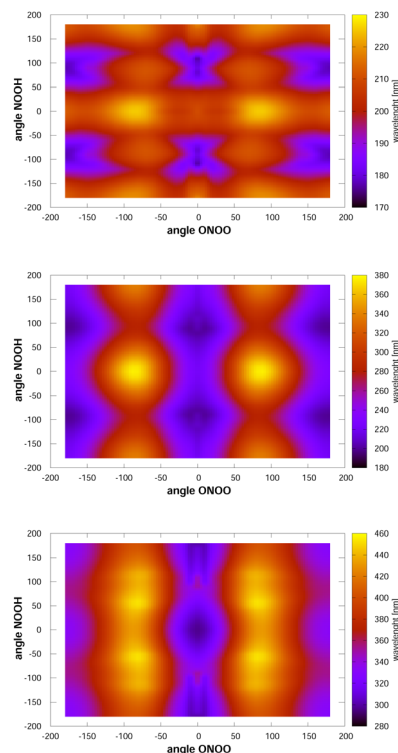


**Fig. 3** Vertical excitation energies between the ground state and the first (lower), second (middle) and third (upper) excited singlet states. Note that the configuration space is covered twice such that the triangles $\tau_{NOOH} \geq \tau_{ONOO}$ and $\tau_{NOOH} \leq \tau_{ONOO}$ represent duplicated configurations. The *cis–cis* conformer is located at the centre. Of the *trans*-perp conformer, which has symmetry $C_1$, two enantiomeric forms exist, see the ESI.† They are at $\tau_{NOOH} \approx 90°$ and $\tau_{NOOH} \approx -90°$ with $\tau_{ONOO} \approx -180°$ using the first triangle.

channel, $HOONO \rightarrow HNO + O_2(a^1\Delta_g)$, may become accessible at much higher energies $\Delta E = 17\,768$ cm$^{-1}$.

The aim of the present work is to understand the photo-decomposition pathways of HOONO in the *cis–cis* and *trans*-perp configurations in the lowest three excited singlet states that were reached in W.-J. Lo and Y. P. Lee's[15] experiment. The asymptotic energies can be obtained from combinations of the product energies according to their electronic states, which are reported in Table 3.

The lowest dissociation channels including those from excited electronic states are thus:

$$NO_2(\tilde{X}^2A_1[A']) + OH(X^2\Pi[A' + A'']) \quad \Delta E = 6925 \text{ cm}^{-1} \quad (4)$$

$$HO_2(\tilde{X}^2A'') + NO(X^2\Pi[A' + A'']) \quad \Delta E = 9548 \text{ cm}^{-1} \quad (5)$$

$$HO_2(\tilde{A}^2A') + NO(X^2\Pi[A' + A'']) \quad \Delta E = 16\,649 \text{ cm}^{-1} \quad (6)$$

$$NO_2(\tilde{A}^2B_2[A']) + OH(X^2\Pi[A' + A'']) \quad \Delta E = 17\,318 \text{ cm}^{-1} \quad (7)$$

In the above expressions, the symmetry labels in the $C_s$ point group are added in parentheses. By correlation, each combination of two fragments gives rise to one state of A′ symmetry and one state of A″ symmetry of HOONO in the *cis–cis* configuration. The *trans*-perp conformer has symmetry $C_1$ and thus all

symmetry labels become A. Both singlet and triplet combinations are allowed. As a result, the electronic ground state and the first excited singlet state have common asymptotes, $NO_2(\tilde{X}^2A_1) + OH(X^2\Pi)$ and $HO_2(\tilde{X}^2A'') + NO(X^2\Pi)$, and the second and third excited electronic singlet states, $NO_2(\tilde{A}^2B_2) + OH(X^2\Pi)$ and $HO_2(\tilde{A}^2A'') + NO(X^2\Pi)$. Dissociation to OH or NO in their first excited states and the triatomics in their electronic ground states only occurs at much higher energy.

To investigate the photodecomposition process, we have run semiclassical trajectories with the Newton-X package[45] starting at an excited singlet state. The initial configurations for a set of 100 trajectories were obtained from a Wigner distribution in

**Table 3** Electronic energies, in cm$^{-1}$, of the decomposition fragments, relative to their electronic ground states. The values for N$O_2$ are taken from Ndengue *et al.*,[47] those for HO$_2$, $\tilde{X}$ and $\tilde{A}$ states, are from Melnikov *et al.*[48] All other data are from NIST[49]

| NO$_2$ + OH channel | | | | HO$_2$ + NO channel | | | |
|---|---|---|---|---|---|---|---|
| NO$_2$ | | OH | | HO$_2$ | | NO | |
| $\tilde{X}^2A_1$ | 0 | $X^2\Pi$ | 0 | $\tilde{X}^2A''$ | 0 | $X^2\Pi$ | 0 |
| $\tilde{A}^2B_2$ | 10393 | $A^2\Sigma^+$ | 32684.1 | $\tilde{A}^2A'$ | 7101 | $A^2\Sigma^+$ | 43965.7 |
| $\tilde{B}^2B_1$ | 14615 | $B^2\Sigma^+$ | 69774 | $\tilde{B}^2A''$ | 48800 | $B^2\Pi$ | 45910 |

**Table 4** The UCAM-B3LYP/maug-cc-pVTZ Mulliken spin densities (SD) and charges ($q$) of the configurations shown in Fig. 4. The atoms are labelled as $H_{(1)}O_{(2)}O_{(3)}N_{(4)}O_{(5)}$. In both channels, neutral fragments with doublet spin symmetry are formed

| Channel | Property | $H_{(1)}$ | $O_{(2)}$ | $O_{(3)}$ | $N_{(4)}$ | $O_{(5)}$ |
|---|---|---|---|---|---|---|
| $H_{(1)}O_{(2)}O_{(3)} + N_{(4)}O_{(5)}$ | SD | −0.01 | 0.23 | 0.78 | −0.71 | −0.29 |
| | Q | 0.25 | −0.09 | −0.16 | 0.08 | −0.08 |
| $H_{(1)}O_{(2)} + O_{(3)}N_{(4)}O_{(5)}$ | SD | 0.02 | −1.02 | 0.27 | 0.45 | 0.28 |
| | Q | 0.27 | −0.27 | −0.24 | 0.55 | −0.31 |



**Fig. 4** Typical product configurations at the end of the trajectories.

phase space. For each of these trajectories, the potential energy surfaces and non-adiabatic coupling terms were computed on the fly. Finally, the hopping probability for passing from the current potential energy surface to any of the other surfaces is computed according to Tully's[50] fewest switches surface hopping (FSSH) procedure. Decoherence correction with simplified decay of mixing[51] was applied. Potential energy surfaces and coupling terms were obtained with the time-dependent density functional theory (TD-DFT) formalism as implemented in Gaussian G16[43] and also at the *ab initio* CASSCF level using Molpro.[42] For computational reasons, two different basis sets had to be used, both of them were of triple-zeta quality. In the Molpro calculations,§ a large CAS(16e,13o) was used together with the diffuse 6-311++G(3df,3pd) segmented basis set, which is approximately equivalent to the aug-cc-VTZ basis. However, the latter basis set cannot be handled by the Cadpac gradient programme within Molpro to compute state-averaged MCSCF gradients. In the TD-DFT calculations, the minimally augmented maug-cc-pVTZ basis set was chosen. This basis set is recommended for DFT calculations[53] as it yields results of almost aug-cc-pVTZ quality at a significantly lower computational cost.

Dissociation of peroxynitrous acid in two fragments of doublet spin multiplicity is intrinsically a multi-reference problem, and thus the MCSCF approach is well suited. However, trajectory calculations at the MCSCF level become rapidly prohibitive in terms of CPU time, in particular if four electronic states are considered simultaneously. Fortunately, it is not necessary to follow the trajectories until "complete" separation of the fragments in order to identify the final products. In the present work, we have found that up to intermediate distances the open-shell singlet system is also described well by density functional theory. This can be seen from the Mulliken charges and spin densities presented in Table 4 for one exemplary product configuration, Fig. 4, of each of the two dissociation channels.

After some experimentation, we chose the CAM-B3LYP functional, developed by Tanai *et al.*,[54] for better description of charge-transfer processes. For our problem, CAM-B3LYP improves the stability of the trajectory propagation compared to B3LYP.

The trajectories were run over $t_{max}$ = 100 fs with a propagation step of $t_{max}$ = 0.25 fs. Visual analysis of the molecular structures along the trajectories did not show a single case in which the fragments would rejoin. On this basis, we attributed the fragments to one of the channels, NO$_2$ + OH or HO$_2$ + NO, depending on whether the O–O or O–N distances were increased by at least 25%

§ A Molpro-Newton-X interface was provided by Alex Brown and Zhibo Wang.[52]

**Table 5** Photolysis product distribution, or quantum yields, following UV excitation to the excited singlet states 1, 2 or 3. 100 trajectories were run for each excited state. The CAM-B3LYP results were obtained with the maug-cc-pVTZ basis set. The MCSCF computations used either the CAS(16e,13o), upper entry, or the CAS(16e,11o), lower entry, active space and the 6-311++G(3df,3pd) basis set, and the small CAS for the first excited state only

| | CAM-B3LYP | | MCSCF | |
|---|---|---|---|---|
| Exc. state | HO$_2$ + NO | NO$_2$ + OH | HO$_2$ + NO | NO$_2$ + OH |
| *Cis–cis* | | | | |
| 1 | 0.95 ± 0.04 | 0.05 ± 0.04 | 0.71 ± 0.09 | 0.29 ± 0.09 |
| | | | 0.92 ± 0.05 | 0.08 ± 0.05 |
| 2 | 0.66 ± 0.09 | 0.34 ± 0.09 | 0.57 ± 0.10 | 0.43 ± 0.10 |
| 3 | 0.32 ± 0.09 | 0.68 ± 0.09 | — | — |
| *Trans*-perp | | | | |
| 1 | 1.00 | 0.00 | 1.00 | 0.00 |
| | | | 1.00 | 0.00 |
| 2 | 0.84 ± 0.07 | 0.16 ± 0.07 | 0.87 ± 0.06 | 0.13 ± 0.06 |
| 3 | 0.56 ± 0.10 | 0.44 ± 0.10 | — | — |

of their initial values. Trajectories that did not satisfy these conditions were analysed manually. The product distributions, or quantum yields, are collected in Table 5. Error bounds were obtained by a statistical analysis, and the results are reported as $p \pm z\sqrt{p(1-p)/n}$, where $p$ denotes the fraction of trajectories leading to a particular channel and $n$ is the total number of trajectories. $z$ = 1.96 for the 95% confidence interval. A small difference was found in the product distributions for the *cis–cis* conformer following excitation to the first excited state. With the larger CAS(16e,13o), a larger yield of NO$_2$ + OH is found. The two additional molecular orbitals in the active space, when compared with the smaller CAS(16e,11o), orbitals 20 and 21, both have antibonding O–O characters. Apparently, their inclusion facilitates the O–O bond rupture. The TD-DFT calculation gives the same product distribution as the small CAS. For other cases, the results are practically the same. With respect to the third excited state, only the TDDFT method was computationally feasible.

## 4 Rate constant for actinic photodecomposition

Photo-decomposition of peroxynitrous acid may occur in the troposphere induced by absorption of sunlight. The unimolecular decay constant with the formation of a product $A$, $J_A$, can be computed as

$$J_A = \int_{\lambda_{min}}^{\lambda_{max}} F(\lambda)\sigma(\lambda)\phi_A(\lambda)\mathrm{d}\lambda \qquad (8)$$

where $F(\lambda)$ is the actinic flux, $\sigma(\lambda)$ is the absorption cross section

**Table 6** Photolysis rate constants, in s$^{-1}$, for the lowest excited singlet state. Note that excitation to higher excited states does not take place in the atmosphere. Initial conditions for $T$ = 220 K were applied. Furthermore, the computed cross-section for the cis–cis conformer was shifted by 20 nm to make the maximum coincide with the experimental maximum. In the case of the trans-perp conformer, a shift of 5 nm did not alter the result. The CAM-B3LYP results were obtained with the maug-cc-pVTZ basis set. The MCSCF computations used a CAS(16e,13o) and the 6-311++G(3df,3pd) basis set

| | CAM-B3LYP | | MCSCF | |
|---|---|---|---|---|
| Exc. state | HO$_2$ + NO | NO$_2$ + OH | HO$_2$ + NO | NO$_2$ + OH |
| *Cis–cis* 1 | $3.89 \times 10^{-4}$ | $8.13 \times 10^{-7}$ | $4.93 \times 10^{-4}$ | $1.26 \times 10^{-4}$ |
| *Trans*-perp 1 | $1.26 \times 10^{-3}$ | — | $1.14 \times 10^{-3}$ | — |

and $\phi_A(\lambda)$ is the quantum yield. The quantum yield, $\phi_A(\lambda)$, is defined as the relative yield of product A as a function of the UV wavelength. For the practical evaluation of the integral in eqn (8), the $\lambda$ interval covered by the trajectories was split into $n$ equal parts, which we call bins,

$$J_A = \sum_{i=1}^{n} \int_{\lambda_{\min,i}}^{\lambda_{\max,i}} F(\lambda)\sigma(\lambda)\phi_A(\lambda)\mathrm{d}\lambda \qquad (9)$$

and the relative yield of product A was determined for this wavelength interval. In the present work, we used $n$ = 5 bins. The actinic flux was taken from the site of the National Center for Atmospheric Research in Boulder.¶ Since ozone absorbs most of the UV-radiation arriving from the sun, only the spectral range between approximately 280 nm and 360 nm is important. Therefore, only excitations to the first excited singlet state take place. The computed rate constants are collected in Table 6.

In thermal equilibrium at room temperature, 99.9% of peroxynitrous acid is found in the cis–cis form. The trans-perp configuration can therefore be neglected in atmospheric modelling. The photolysis rate constant $J$, adding up contributions from the two decay channels, *i.e.* $J = J_{\mathrm{HO_2+NO}} + J_{\mathrm{NO_2+OH}}$, is about $J \approx 6 \times 10^{-4}$ s$^{-1}$ at the MCSCF level. This rate constant may be compared with the unimolecular thermal decay rate constant on the electronic ground state into OH + NO$_2$, for which Golden, Barker and Lohr[7] report $k_{\mathrm{uni}} \approx 10^{-6}$ s$^{-1}$ in the region around the tropopause at about 10 km of altitude, with $T \approx 220$ K and $p \approx 0.26$ bar. Photolysis is thus the principal atmospheric decomposition mechanism of peroxynitrous acid and must be included in atmospheric modelling.

## 5 Conclusions

In the present work, we have reanalysed the experimental UV spectrum of peroxynitrous acid recorded by W.-J. Lo and Y. P. Lee[15] forty years ago. Their broad signals result from excitations to the second excited singlet state, with smaller, overlapping contributions from the third electronic state. Excitation to the first excited state appears in the long-wavelength tail region and was not resolved in the experiment. Since the excited electronic states are repulsive, the molecule will disintegrate upon UV absorption, and the decomposition mechanism was investigated in the present work. In contrast to thermal decomposition, which mainly yields NO$_2$ + OH, the principal photolysis products are HO$_2$ + NO. In the earth's atmosphere, only excitation to the first excited singlet state occurs, as higher-energy solar radiation is absorbed in the ozone layer. The rate constant for atmospheric photodecomposition, which is urgently needed for use in atmospherical models,[7,10,41] was computed here for the first time. Our results show that under conditions near the tropopause and above, photodecomposition is significantly more rapid than thermal decomposition, $J \approx 6 \times 10^{-4}$ s$^{-1}$, whereas $k \approx 10^{-6}$ s$^{-1}$ near the tropopause.[7]

## Author contributions

All authors contributed equally to this work. W. C. is a PhD student supervised by the other three authors.

## Conflicts of interest

There are no conflicts to declare.

## Notes and references

1 B. Finlayson-Pitts and J. James Pitts, *Chemistry of the Upper and Lower Atmosphere: Theory, Experiments, and Applications*, 2000.
2 P. J. Crutzen, *Q. J. R. Meteorol. Soc.*, 1970, **96**, 320–325.
3 C. F. Williams, S. K. Pogrebnya and D. C. Clary, *J. Chem. Phys.*, 2007, **126**, 154321.
4 J. Troe, *J. Phys. Chem. A*, 2012, **116**, 6387–6393.
5 D. Amedro, M. Berasategui, A. J. C. Bunkan, A. Pozzer, J. Lelieveld and J. N. Crowley, *Atmos. Chem. Phys.*, 2020, **20**, 3091–3105.

¶ https://www.acom.ucar.edu/Models/TUV/Interactive_TUV/

**128** | *Phys. Chem. Chem. Phys.*, 2024, **26**, 123–129

This journal is © the Owner Societies 2024

6  B. D. Bean, A. K. Mollner, S. A. Nizkorodov, G. Nair, M. Okumura, S. P. Sander, K. A. Peterson and J. S. Francisco, *J. Phys. Chem. A*, 2003, **107**, 6974–6985.

7  D. M. Golden, J. R. Barker and L. L. Lohr, *J. Phys. Chem. A*, 2003, **107**, 11057–11071.

8  H. Hippler, S. Nasterlack and F. Striebel, *Phys. Chem. Chem. Phys.*, 2002, **4**, 2959–2964.

9  A. K. Mollner, S. Valluvadasan, L. Feng, M. K. Sprague, M. Okumura, D. B. Milligan, W. J. Bloss, S. P. Sander, P. T. Martien, R. A. Harley, A. B. McCoy and W. P. L. Carter, *Science*, 2010, **330**, 646–649.

10  F. A. F. Winiberg, K. Zuraski, Y. Liu, S. P. Sander and C. J. Percival, *J. Phys. Chem. A*, 2020, **124**, 10121–10131.

11  D. A. Dixon, D. Feller, C.-G. Zhan and J. S. Francisco, *J. Phys. Chem. A*, 2002, **106**, 3191–3196.

12  Y. Zhao, K. N. Houk and L. P. Olson, *J. Phys. Chem. A*, 2004, **108**, 5864–5871.

13  D. J. Benton and P. Moore, *J. Chem. Soc. A*, 1970, 3179–3182.

14  B. M. Cheng, J. W. Lee and Y. P. Lee, *J. Phys. Chem.*, 1991, **95**, 2814–2817.

15  W. Lo and Y. P. Lee, *J. Chem. Phys.*, 1994, **101**, 5494–5499.

16  W.-J. Lo and Y.-P. Lee, *Chem. Phys. Lett.*, 1994, **229**, 357–361.

17  M. P. McGrath, M. M. Francl, F. S. Rowland and W. J. Hehre, *J. Phys. Chem.*, 1988, **92**, 5352–5357.

18  X. Zhang, M. R. Nimlos, G. B. Ellison, M. E. Varner and J. F. Stanton, *J. Chem. Phys.*, 2006, **124**, 084305.

19  X. Zhang, M. R. Nimlos, G. B. Ellison, M. E. Varner and J. F. Stanton, *J. Chem. Phys.*, 2007, **126**, 174308.

20  N. M. Donahue, R. Mohrschladt, T. J. Dransfield, J. G. Anderson and M. K. Dubey, *J. Phys. Chem. A*, 2001, **105**, 1515–1520.

21  S. A. Nizkorodov and P. O. Wennberg, *J. Phys. Chem. A*, 2002, **106**, 855–859.

22  I. B. Pollack, I. M. Konen, E. X. J. Li and M. I. Lester, *J. Chem. Phys.*, 2003, **119**, 9981–9984.

23  J. L. Fry, S. A. Nizkorodov, M. Okumura, C. M. Roehl, J. S. Francisco and P. O. Wennberg, *J. Chem. Phys.*, 2004, **121**, 1432–1448.

24  E. X. J. Li, I. M. Konen, M. I. Lester and A. B. McCoy, *J. Phys. Chem. A*, 2006, **110**, 5607–5612.

25  B. J. Drouin, J. L. Fry and C. E. Miller, *J. Chem. Phys.*, 2004, **120**, 5505–5508.

26  J. L. Fry, B. J. Drouin and C. E. Miller, *J. Chem. Phys.*, 2006, **124**, 084304.

27  M. P. McGrath and F. S. Rowland, *J. Phys. Chem.*, 1994, **98**, 1061–1067.

28  M. P. McGrath and F. S. Rowland, *J. Chem. Phys.*, 2005, **122**, 134312.

29  R. Sumathi and S. D. Peyerimhoff, *J. Chem. Phys.*, 1997, **107**, 1872–1880.

30  R. S. Zhu and M. C. Lin, *J. Chem. Phys.*, 2003, **119**, 10667–10677.

31  R. D. Bach, O. Dmitrenko and C. M. Estévez, *J. Am. Chem. Soc.*, 2003, **125**, 16204–16205.

32  H. W. Jin, Z. Z. Wang, Q. S. Li and X. R. Huang, *J. Mol. Struct.: THEOCHEM*, 2003, **624**, 115–121.

33  C. Chen, B. C. Shepler, B. J. Braams and J. M. Bowman, *J. Chem. Phys.*, 2007, **127**, 104310.

34  P. Szakács, J. Csontos, S. Das and M. Kállay, *J. Phys. Chem. A*, 2011, **115**, 3144–3153.

35  J. Matthews, A. Sinha and J. S. Francisco, *J. Chem. Phys.*, 2004, **120**, 10543–10553.

36  I. M. Konen, I. B. Pollack, E. X. J. Li, M. I. Lester, M. E. Varner and J. F. Stanton, *J. Chem. Phys.*, 2005, **122**, 094320.

37  D. P. Schofield, H. G. Kjaergaard, J. Matthews and A. Sinha, *J. Chem. Phys.*, 2005, **123**, 134318.

38  M. A. Boyer and A. B. McCoy, *J. Chem. Phys.*, 2022, **157**, 164113.

39  A. B. McCoy, M. K. Sprague and M. Okumura, *J. Phys. Chem. A*, 2010, **114**, 1324–1333.

40  Y. Li and J. S. Francisco, *J. Chem. Phys.*, 2000, **113**, 7976–7981.

41  D. M. Golden and G. P. Smith, *J. Phys. Chem. A*, 2000, **104**, 3991–3997.

42  H.-J. Werner, P. J. Knowles, G. Knizia, F. R. Manby, M. Schütz, *et al.*, *MOLPRO, version 2021.1, a package of ab initio programs*, 2021, see **https://www.molpro.net**.

43  M. J. Frisch, G. W. Trucks, H. B. Schlegel, G. E. Scuseria, M. A. Robb, *et al.*, *Gaussian-16 Revision C.01*, Gaussian Inc., Wallingford CT, 2016.

44  S. Berski, Z. Latajka and A. J. Gordon, *J. Comput. Chem.*, 2011, **32**, 1528–1540.

45  M. Barbatti, M. Ruckenbauer, F. Plasser, J. Pittner, G. Granucci, M. Persico and H. Lischka, *Wiley Interdiscip. Rev.: Comput. Mol. Sci.*, 2014, **4**, 26–33.

46  M. Barbatti, A. J. A. Aquino and H. Lischka, *Phys. Chem. Chem. Phys.*, 2010, **12**, 4959–4967.

47  S. Ndengué, E. Quintas-Sánchez, R. Dawes and D. Osborn, *J. Phys. Chem. A*, 2021, **125**, 5519–5533.

48  V. V. Melnikov, P. Jensen and T. Hirano, *J. Chem. Phys.*, 2009, **130**, 224105.

49  P. Linstrom and W. Mallard, Proceedings of the 10th International Chemical Information Conference and Exhibition, Nimes, FR, 1998.

50  J. C. Tully, *J. Chem. Phys.*, 1990, **93**, 1061–1071.

51  G. Granucci and M. Persico, *J. Chem. Phys.*, 2007, **126**, 134114.

52  Z. Wang, *Master thesis*, University of Alberta, Department of Chemistry, Supervisor Alex Brown, 2019.

53  E. Papajak, H. R. Leverentz, J. Zheng and D. G. Truhlar, *J. Chem. Theory Comput.*, 2009, **5**, 1197–1202.

54  T. Yanai, D. P. Tew and N. C. Handy, *Chem. Phys. Lett.*, 2004, **393**, 51–57.

This journal is © the Owner Societies 2024

*Phys. Chem. Chem. Phys.*, 2024, **26**, 123–129 | 129